

Original article

Influence of the temperature on the band-gap energy of reduced graphene-oxide nanoplatelets described with the Varshni model

Influencia de la temperatura en la brecha energética de nanoplaquetas de óxido de grafeno reducido según el modelo de Varshni

 John Jairo Prías-Barragán

Programa de Doctorado en Ciencias Física, Programa de Tecnología en Instrumentación Electrónica, Instituto Interdisciplinario de las Ciencias, Universidad del Quindío, Colombia

Inaugural article as Correspondent Member of the Colombian Academy of Exact, Physical and Natural Sciences

Abstract

The present study estimated the influence of temperature on the band-gap energy in reduced graphene oxide (rGO) nanoplatelets obtained from bamboo. Individual rGO nanoplatelets were synthesized via double thermal decomposition (DTD) in a pyrolysis system under a controlled nitrogen atmosphere and carbonization temperature fixed at $T_{CA} = 973$ K. For the electrical characterization of individual rGO nanoplatelets, the I-V curves method was used at four electrical contacts of Pt nano-wires grown by focused electron-ion beam induced deposition (FEBID) system. The influence of temperature on the band-gap energy ($E_g(T)$) was estimated via electrical resistivity measurements taken at different temperatures varying from 30 to 290 K. As regards the electrical properties, the rGO samples exhibited an electrical response at room temperature, acting as a narrow band-gap semiconductor with a band-gap energy value of 0.11 eV and an electrical response at low temperature described mainly by the Mott 3-dimensional variable range hopping (VRH-3D) model. The $E_g(T)$ dependence was analyzed considering the Varshni, Bose-Einstein, Magnoogian-Wooley, Viña, *et al.*, and Päsler phenomenological models. The Varshni model adequately described the $E_g(T)$ behavior with extrapolated $E_g(T = 0$ K) value at 0.292 eV and Varshni parameters at $\alpha = 6.70 \times 10^{-4}$ eV/K and $\beta = 33.62$ K. These values agree with the known order of magnitude of the Varshni coefficients reported for other narrow band-gap semiconductors such as InAs and InSb. Hydroxyl bridges on rGO were found modifying carbon-carbon bond length and controlling electrical responses, as previously reported when employing first-principle calculations via the density functional theory (DFT). These results suggest that individual rGO nanoplatelets can be excellent materials for developing advanced electronics for sensors and devices.

Keywords: Reduced graphene oxide; Nanoplatelets; Band-gap energy; HR-TEM.

Resumen

Se estimó la dependencia de la temperatura con la energía de banda prohibida ($E_g(T)$) en nanoplaquetas individuales de grafeno oxidado reducido (rGO) obtenidas de bambú. Las rGO se sintetizaron mediante el método de la doble descomposición térmica en un sistema de pirólisis, bajo una atmósfera de nitrógeno controlada y temperatura de carbonización fija en $T_{CA} = 973$ K. Para la caracterización eléctrica de las rGO se empleó el método de curvas I-V en cuatro contactos eléctricos con nanocables de Pt depositados mediante el sistema de deposición inducida por haces enfocados de electrones e iones. La $E_g(T)$ se estimó usando medidas de resistividad eléctrica tomadas a temperaturas que variaban entre los 30 y los 290 K. Las rGO exhibieron una $E_g(T)$ descrita principalmente por el modelo de Mott de salto de rango variable tridimensional (VRH-3D). La $E_g(T)$ se analizó considerando los modelos fenomenológicos de Varshni, Bose-Einstein, Magnoogian-Wooley, Viña, *et al.*, y Päsler. Se encontró que el modelo de Varshni describía adecuadamente el comportamiento experimental de la $E_g(T)$, con el valor de $E_g(T = 0$ K) extrapolado a 0,292 eV y los parámetros de

Citation: Prías-Barragán JJ. Influence of the temperature on the band-gap energy of reduced graphene-oxide nanoplatelets described with the Varshni model. Revista de la Academia Colombiana de Ciencias Exactas, Físicas y Naturales. 47(185):807-821, octubre-diciembre de 2023. doi: <https://doi.org/10.18257/raccefyfyn.2008>

Editor: Gabriel Téllez Acosta

Corresponding autor:

Jhon Jairo Prías-Barragán;
jjprias@uniquindio.edu.co

Received: September 12, 2023

Accepted: November 30, 2023

Published on line: December 14, 2023



This is an open access article distributed under the terms of the Creative Commons Attribution License.

Varshni de $\alpha = 6,70 \times 10^{-4}$ eV/K y $\beta = 33,62$ K. Estos valores concuerdan con el orden de magnitud de los coeficientes de Varshni reportados para otros semiconductores de banda prohibida estrecha como el InAs y el InSb. Asimismo, se encontró que la presencia de puentes de hidroxilo en la rGO modificaba la longitud de los enlaces carbono-carbono, lo cual domina la respuesta eléctrica, como se preveía y ha sido reportado previamente al emplear cálculos de primeros principios vía la teoría del funcional de la densidad (DFT). Estos resultados sugieren que las rGO pueden ser excelentes materiales para el desarrollo de la electrónica avanzada de sensores y dispositivos.

Palabras claves: Grafeno oxidado reducido; Nanoplaquetas; Energía de banda prohibida; HR-TEM.

Introduction

In recent years, the interest in rGO has grown, given the relevance of graphene and graphene oxide for science and technological applications (**Geim & Novoselov**, 2007; **Novoselov et al.**, 2005; **Novoselov et al.**, 2004; **Jiang et al.**, 2014). Graphite oxide (GO) has received attention for its use as a source of graphene oxide by exfoliation techniques. Reduced graphene oxide has surface properties and a layered structure that makes it a versatile material for applications (**Jiang et al.**, 2014; **Sachdeva et al.**, 2020; **Kigozi et al.**, 2020; **Benevides et al.**, 2020; **Fenfen et al.**, 2020; **Wang et al.**, 2020; **Faiz et al.**, 2020; **Mizoguchi et al.**, 2020; **Abbas et al.**, 2020; **Naser et al.**, 2020; **Newman et al.**, 2020). The physicochemical properties of GO can be modified and functionalized by tuning its oxide composition and crystal structure. With an oxide coverage of $< 10\%$, it is possible to obtain rGO. Reduced GO platelets can be obtained as micro-platelets and nanoplatelets decorated mainly with multifunctional groups, i.e., hydroxyl bridges and epoxy groups that can dominate the physical transport properties on rGO given that oxides get the out-plane carbon atoms from the basal graphene plane, inducing defects and imperfections on its surface that dominate rGO nature (**Geng et al.**, 2009; **Hoyos-Ariza et al.**, 2023). Transport properties can be influenced in these platelets can be influenced by the multilayered configuration, and the π -bond delocalization can produce van der Waals forces between the induced electric dipoles (**Rozploch et al.**, 2007) and the defects (**He et al.**, 2011). All these effects can be profited in advanced thermo-electrical, electronic, magnetic, optical, photomechanical, and electro-optical devices and sensors (**Tang et al.**, 2008). GO platelets can be used in batteries (**Kim et al.**, 2012; **Prusty & Swain**, 2012; **Matsuo & Ueda**, 2014; **Zou et al.**, 2015), electrical energy storage (**Lobato et al.**, 2014; **Singh & Chandra**, 2013), advanced electronic sensors and devices (**Ghosh et al.**, 2014; **Wei et al.**, 2009; **Zhang et al.**, 2012; **Llatser et al.**, 2012; **Mishra & Ramaprabhu**, 2012; **Grande et al.**, 2012; **Sangwan et al.**, 2011; **He & Tjong**, 2013), catalysis (**Geng et al.**, 2014), metal sorption (**Petit & Badosz**, 2015), hydrogen storage (**Xue et al.**, 2014), carbon dioxide sorption (**Arango-Hoyos et al.**, 2023), and to obtain graphene oxide (**Liu et al.**, 2015; **Jia et al.**, 2014; **Kyzas et al.**, 2014; **Tang et al.**, 2012).

Graphite oxide and rGO can be obtained by the traditional methods of Brodies (**Jia et al.**, 2014), Hummers (**Kyzas et al.**, 2014), or Tang Lau (**Tang et al.**, 2012) or by their modified versions.

However, these methods yield only micron-sized graphene flakes, require strong oxides (Brodie and Hummer methods) or glucose (Tang Lau method), and are time consuming. Although they are excellent for basic research, the GO obtained with these methods decomposes at temperatures between 553 and 573 K, becoming amorphous carbon and losing many oxides. The thermal decomposition method employing a pyrolysis system is a low-cost and eco-friendly alternative to synthesize graphene oxide multilayers such as the nanoplatelets from bamboo using pyrolytic acid (BPA) as source material at higher temperatures: from 573 to 973 K, which differs from the traditional methods as previously reported by **Prías-Barragán et al.** (2015-2022). The composition, stage structure, defects, and graphitization degree of rGO depend on the carbonization temperature (TCA): higher temperatures promote the elimination of organic compounds and oxygen functional groups leading to the improvement of the crystal structure with a positive impact on the thermal,

electrical, and magnetic transport (**Kuzemsky**, 2013; **Rao**, 2012; **Makarova et al.**, 2011; **Virendra et al.**, 2011; **Gross et al.**, 2016). TCA at 973 K in the DTD method leads to a reduction of oxygen contents to 5.3% and an increase in electrical conductivity of nearly two orders of magnitude as evidenced by preliminary electrical measurements performed on individual nanoplatelets (**Prías-Barragán et al.**, 2022; **Gross et al.**, 2016). The thermal conductivity of rGO platelets is also expected to reduce when oxygen contents decrease, as reported in graphene oxide (**Gross et al.**, 2016; **Mu et al.**, 2014), which may be convenient for electronic applications. Electrical conductivity and oxygen concentration are strongly correlated in rGO; it has been shown that by increasing the rGO reduction level, *i.e.*, by restoring sp^2 hybridization, room temperature conductivity tends to increase (**Geng et al.**, 2009; **He et al.**, 2011; **Tang et al.**, 2008; **Petit & Badosz**, 2015; **Gross et al.**, 2016). Electrical conduction in rGO is mainly due to sp^2 hybridization resulting from delocalized electrons (π orbital) moving freely throughout the graphite structure. Oxygenized areas containing high amounts of carbon domains show hybridized sp^3 that behaves as an insulator. The electrical charge transport mechanism in a landscape of coexisting sp^2/sp^3 regions is akin to that of disordered semiconductors where electron localization and hopping conduction play a significant role. As they depend on oxygen contents, rGO-based materials undergo insulator-semiconductor-semimetal transitions with the reduction. Studies where the sp^2 fraction varies have shown that diverse types of conduction mechanisms occur depending on whether the rGO sheet is slightly or highly reduced (**Xue et al.**, 2014; **Liu et al.**, 2015; **Gross et al.**, 2016).

Regarding the temperature dependence of the electrical conductivity in rGO exhibiting semiconductor-like transport behavior, there are different conduction mechanisms (**Novoselov et al.**, 2004; **Jiang et al.**, 2014; **Rozploch et al.**, 2007). Other authors (**Xue et al.**, 2014; **Gross et al.**, 2016) found that while at a higher temperature regime of well-rGO, thermally excited carriers dominate the conduction, the low-temperature regime has to be described through the Mott variable range hopping (VRH) model. The temperature-dependent longitudinal conductivity described by the VRH model is well-known in all the dimensionalities described in the system (**Gross et al.**, 2016). Thus, the dimensionalities correspond to the Mott VRH conduction mechanism proposed respectively for 2D and 3D systems, without considering the Coulomb interaction. When there is a Coulomb interaction between initial and final hopping sites, Efros and Shklovskii proposed the unidimensional case for the long-range hole-electron interaction at the Fermi level (**Gross et al.**, 2016). Finally, the zero-dimensionality case corresponds to the Arrhenius type for thermal-activated conduction mechanisms. It is worth mentioning that the first three possibilities have also served to analyze charge transport mechanisms in non-crystalline materials (**Gross et al.**, 2016). However, the basic description of the temperature dependence of the energy band gap is an open research question, as suggested by possible rGO applications in temperature sensors (**Árias-Niquepa et al.**, 2019).

Considering rGO nanoplatelets as a narrow band-gap semiconductor (**Prías-Barragán et al.**, 2015-2022; **Gross et al.**, 2016), various models have been proposed to describe the temperature dependence of the band-gap energy in rGO (**Varshni**, 1967; **O'Donnell & Chen**, 1991; **Krystek et al.**, 1995; **Rui et al.**, 2011; **Viña et al.**, 1984; **Pässler**, 1997). In this sense, the present study aims to determine the best model to elucidate temperature dependence of the band-gap energy in rGO nanoplatelet samples. Its results may help further understand the systematic transport mechanism and electrical properties of graphene oxide multilayers as nanoplatelets and their impact on advanced electronic sensors and devices.

Methods

The rGO nanoplatelet samples were synthesized using the double thermal decomposition (DTD) method from bamboo pyrolygneous acid or tar (BPA) in a pyrolysis system under controlled temperature and nitrogen atmosphere at 973 K with a carbonization temperature (TCA), a 5.3% rGO value as oxides coverage estimated using XPS and EDAX measurements, as reported before (**Prías-Barragán et al.**, 2018).

The BPA was obtained from bamboo (*Guadua angustifolia* Kunth, macana biotype) through an initial pyrolysis process at 973 K and collected in a decanting funnel glass where the bamboo tar was easily decanted and separated. Then, the BPA bamboo tar was used as source material for rGO at 973 K. The waste product of the commercial bamboo-*Guadua angustifolia* Kunth was disposed of according to the relevant regulations.

At TCA = 973 K, the thermal decomposition of the aromatic structure of the phenol compounds in the bamboo tar forms carbon structures (Gross *et al.*, 2016); when the BPA or tar carbonization process is completed, carbon foam is obtained and subsequently turned into platelet powders by mechanical grinding with a ceramic hand mortar. The carbonization yield of the rGO sample was around 18%, measured as the quotient between the rGO sample weight after the carbonization process and the pyroligneous acid weight before carbonization. For an overview of these processes and other experimental details, see Prías-Barragán *et al.* (2015-2022).

For the electrical measurement of individual nanoplatelets, the samples were prepared by suspending rGO in isopropanol and then depositing them in the proximity of the metallic contact pads (fabricated firstly by optical lithography) on a SiO₂/Si substrate. Individual nanoplatelets were then located at low voltages (<5 kV) using an SEM system with a focused ion beam (FIB) (Helios 650 model by FEI). The focused ion beam-induced deposition (FIBID) technique was used to deposit four Pt lead wires to connect the nanoplatelets to the metallic contact pads where the micro-probes were positioned. The Pt-based contacts deposited optimally by FIBID allowed low contact resistivity to perform noise-free electrical characterization of micro- or nanostructures (Gross *et al.*, 2016; Kajen *et al.*, 2013; Mineo *et al.*, 2013). For additional details on this technique, see Gross *et al.* (2016).

The SEM images of the experimental setup displaying the microprobes, the metallic contact pads, and the Pt wires on individual rGO nanoplatelets as reported (Gross *et al.*, 2016). For the electrical measurements, current in a range of $\pm 6 \mu\text{A}$ was injected on the two external contacts using a Keithley 6220 DC current source, while the voltage was measured at the two internal contacts with a Keithley 2182 A nanovoltmeter. Temperature-dependent measurements of the resistance were registered inside a vacuum chamber using a closed-cycle Helium cryostat system.

The Raman measurements were registered with a Horiba Jobin Yvon micro-Raman spectrometer, model Labram HR. All spectra were collected in the backscattering configuration and excited with visible laser light at 532 nm wavelength. The spectra were recorded with a 600 line/mm grating. A 50 X objective was used to focus the excitation laser light on the right spot of the GO samples. The sample temperature was controlled using a cold-hot cell operated with a liquid nitrogen source in a Linkam accessory. Precautions were taken to avoid local heating of the samples by the excitation laser, so all measurements were performed at low excitation power. The power on top of the cold-hot cell window was below 4.8 mW (correspondingly, much smaller on the sample surface). The estimated accuracy of the cell temperature control was around 0.1 °C. All spectra were obtained under the same conditions from 1000 to 4000 cm⁻¹. X-ray diffraction patterns were obtained using a Panalytical Systems diffractometer with Cu K α radiation ($\alpha = 1.542 \text{ \AA}$).

The morphological and compositional characteristics of rGO nanoplatelets were examined using scanning electron microscopy (SEM) and energy-dispersive X-ray spectroscopy (EDS) with a Phenom G2 Pro Microscopy field-emitting scanning electron microscope. Transmission electron microscopy (TEM) and high-resolution (HR)-TEM images were obtained with a Tecnai F20 Super Twin TMP on an FEI microscope operating at 80 kV and equipped with a Cs image corrector and a Gatan Tridiem spectrometer. The oxide coverage composition of GO nanoplatelet samples was measured using the XPS technique in an XPS Spectrometer Kratos AXIS Supra system considering an X-ray Source Mono Al K α 225 W (15 mA/15 kV), low pressure of 10⁻⁹ Torr, analysis of an initial area of 700 × 300 μm^2 , and a depth profile at 110 μm of diameter, a pass energy/step width of

160 eV/1000 meV at regions of 20 eV/100 meV (200 meV in CKLL), an ion milling at GCIB 2.5 keV Ar 500+, and a charge neutralizer. Relative hybridizations (sp² and sp³) were determined from the carbon Auger signal at CKLL contributions.

Theory

The band-gap energy can depend on temperature, which can describe different phenomenological models for $E_g(T)$. Some expressions for $E_g(T)$ are the Varshni, Bose-Einstein, Magnoogian-Wooley, Viña, and Pässler models. The Varshni empirical expression describes temperature dependence on the band-gap energy in semiconductors (Varshni, 1967; O'Donnell & Chen, 1991; Krystek *et al.*, 1995; Chen *et al.*, 2011; Viña *et al.*, 1984; Pässler, 1997):

$$E_g(T) = E_g(0) - \left(\frac{\alpha T^2}{T + \beta} \right) \quad (1),$$

where $E_g(0)$ is the extrapolated band-gap energy value at zero temperature; α and β are fitting parameters characteristic of a given material (Varshni, 1967; O'Donnell & Chen, 1991; Krystek *et al.*, 1995; Chen *et al.*, 2011; Viña *et al.*, 1984; Pässler, 1997). This model considers the temperature effect on the band-gap energy, but the Varshni coefficients offer a few physics descriptions of the carriers or exciton interactions involved in some semiconductors whereby the Bose-Einstein model considers these effects in $E_g(T)$.

The Bose-Einstein model obtained from considering the 3N oscillator theory of the specific heat problem considers the free charge carriers or exciton interactions with the phonon average participant, and it has the following functional form (O'Donnell & Chen, 1991):

$$E_g(T) = E_g(0) - \left(\frac{2a_B}{\exp\left(\frac{\theta_B}{T}\right) - 1} \right) \quad (2),$$

where $E_g(0)$ is the extrapolated band-gap energy value at zero temperature; a_B and θ_B are the fitting parameters characteristic of a given material related to the coupling strength between the charge carrier and the excitons and the average characteristic temperature of the phonon participant (optical or acoustic phonon), respectively. This model does not consider the lattice dilation contribution in $E_g(T)$ whereby the Magnoogian-Wooley model appears.

The Magnoogian-Wooley expression considers the effect of thermal expansion and electron-phonon interaction in the band-gap energy, and it is given by (Krystek *et al.*, 1995):

$$E_g(T) = E_g(0) + UT^s + V\theta \left[\coth\left(\frac{\theta}{2T}\right) - 1 \right] \quad (3),$$

where the first term, $E_g(0)$, is the band-gap at $T = 0$ K; the second term represents the lattice dilation with U as the lattice dilation coefficient; s describes the average exciton-phonon coupling strength, and the third term is related to the electron-phonon interaction; V is the temperature-dependent shift in the band-gap, and θ is the temperature-related parameter. The fitting parameters U , s , and θ are independent of the temperature (Chan, 2011). As expression (3) has five fitting parameters, a similar model with lower fitting parameters was proposed in the Viña expression.

Viña *et al.* (1984) fitted data on the critical-point energies of germanium to the Varshni relation, pointing out that they can also fit these data to an expression where the energy thresholds decrease proportionally to the Bose-Einstein statistical factors for phonon emission plus absorption and proposing that:

$$E_g(T) = E_g(0) - b \left[1 + \frac{2}{\exp\left(\frac{\theta}{T}\right) - 1} \right] \quad (4),$$

where b is an energy factor related to the phonon emission plus absorption and θ is the temperature-related parameter. The term within the brackets in expression (4) readily reduces to $\coth(\theta/2T)$ so that equation (4) can be written in a form comparable to

expression (3). Equation (4) describes $E_g(T)$ in terms of the Bose-Einstein statistical factors for phonon emission plus absorption via exponential factor. Another interpretation of $E_g(T)$ in terms of the power law was proposed by the Pässler model (Pässler, 1997).

The Pässler expression has another focus regarding the temperature-dependent band-gap energy, $E_g(T)$, that resorts to the power law behavior for phononic contribution (Pässler, 1997):

$$E_g(T) = E_g(0) - \alpha_p \theta \left[\sqrt[p]{1 + \left(\frac{2T}{\theta}\right)^p} - 1 \right] \quad (5),$$

where $E_g(T)$ is the band-gap energy at 0 K; α_p is a factor that represents the strength of the phononic contribution; θ is the effective phonon temperature, and exponent p relates to the symmetry of the phononic contribution to the band-gap energy. In this section, the $E_g(T)$ different models were compared as given in expressions (1-5) describing the experimental data of temperature dependence on the band-gap energy in rGO samples.

Results and discussion

Figure 1 shows the morphology analysis in individual rGO nanoplatelets using HR-TEM. As shown in **Figure 1a** TEM of individual rGO nanoplatelets, there is a high electron transparency associated with lower thickness (~ 60 nm); the graphitic plate formations and high electron transparency are expected in graphite material. The thickness was 60 nm and the lateral dimensions were $10 \mu\text{m}$, which agree with the nanoplatelets dimensions in the ISO/TS 27687:2008 technical specifications (ISO Technical specification, 2008). The HR-TEM in **Figure 1b** shows local graphene formations, defects, and impurities of oxygen and hydrogen (sp^2 and sp^3) domains identified by EDS, FTIR, and EELS (Gross *et*

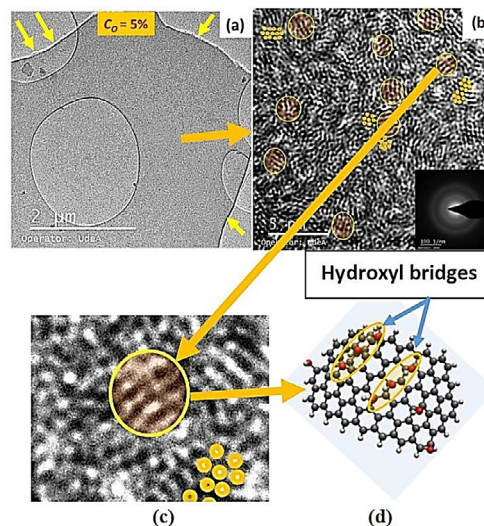


Figure 1. Morphology of individual rGO nanoplatelet: **(a)** TEM image of rGO nanoplatelet presents lateral dimensions and thickness of $10 \mu\text{m}$ and 60 nm, respectively. The TEM image shows graphitic plate-type formations (HR in white representing surface position used in high-resolution mode); the yellow arrows indicate the nanoplatelet border. **(b)** HR-TEM image shows the expected graphene formations on the surface of a single graphene oxide nanoplatelet. The inset of **(b)** corresponds to electron diffraction pattern results as diffuse rings revealing the polycrystalline structure of the rGO sample. **(c)** Negative zoom image from HR-TEM showing graphene formations, impurities, defects in patterns formed by the parallel lines associated with the presence of hydroxyl bridges (Prías-Barragán *et al.*, 2022; Hoyos-Ariza *et al.*, 2023) and the patterns presented in **Figure 1d**. **(d)** The structure of rGO simulated by first principle calculations via DFT shows atomic patterns of parallel lines, which can be attributed to hydroxyl bridges induced by hydrogen atom interactions with neighboring oxygen atoms.

et al., 2016) with a random distribution on the surface of the graphite oxide nanoplatelets and carbon-oxygen and carbon-hydrogen bonds, such as epoxy and hydroxyl bridges (Prías-Barragán *et al.*, 2022; Hoyos-Ariza *et al.*, 2023), that can make carbon atoms exit out-plane and generate local corrugation defects (local deformation of the graphene layers) of great interest in the study of the magnetic properties of carbon materials resulting from electron delocalization, as reported (Kuzemsky, 2013; Rao *et al.*, 2012; Makarova *et al.*, 2011; Virendra *et al.*, 2011; Gross *et al.*, 2016). The inset in figure 1b shows the electron diffraction pattern revealing the polycrystalline structure of the rGO sample as given by the diffuse rings observed experimentally.

Figure 1c shows a negative zoom image of graphene formations related to the rGO structure simulated computationally, as shown in figure 1d, with the hydroxyl bridge forming parallel lines as large-scale patterns, possibly due to hydrogen atoms interactions with oxygen atoms (Prías-Barragán *et al.*, 2022; Hoyos-Ariza *et al.*, 2023) using first principle calculations via the density functional theory. This computational simulation of the rGO structure exhibits the same band-gap energy value as the experimental one measured here in an individual rGO nanoplatelet sample (Hoyos-Ariza *et al.*, 2023). Local corrugation defects in the rGO structure are observed; this behavior can be attributed to the hydroxyl bridge in the C-OH groups (Figure 1d) corroborated by EDAX, FTIR spectra, and XRD results previously reported (Prías-Barragán *et al.*, 2016-2022).

In figure 2a, the geometric structural dimensions in graphite and rGO samples are compared as determined via X-ray diffraction spectra analysis; in rGO samples, the presence of multifunctional oxide increases the geometric dimensions in rGO structures, as expected. Previously, we reported an rGO sample (TCA = 973 K) with a sp² domain (O-H and C-O-C groups) at around 66% and a sp³ domain (C-H group) at 34% as determined by EELS (Gross *et al.*, 2016). Figure 2b shows the typical Raman spectra of rGO samples (Prías-Barragán *et al.*, 2016).

In figure 2b, the Raman spectra analyses were carried out using a theoretical fitting with six Lorentzian function contributions associated with a G-band peak at 1550 cm⁻¹ (from 1550 to 1580 cm⁻¹), indicating the formation of a graphitized structure by the vibration of sp² bonded carbon atoms, a D-band peak of around 1330 cm⁻¹ (from 1330 to 1360 cm⁻¹) corresponding to the disorder-induced phonon mode by defect presence

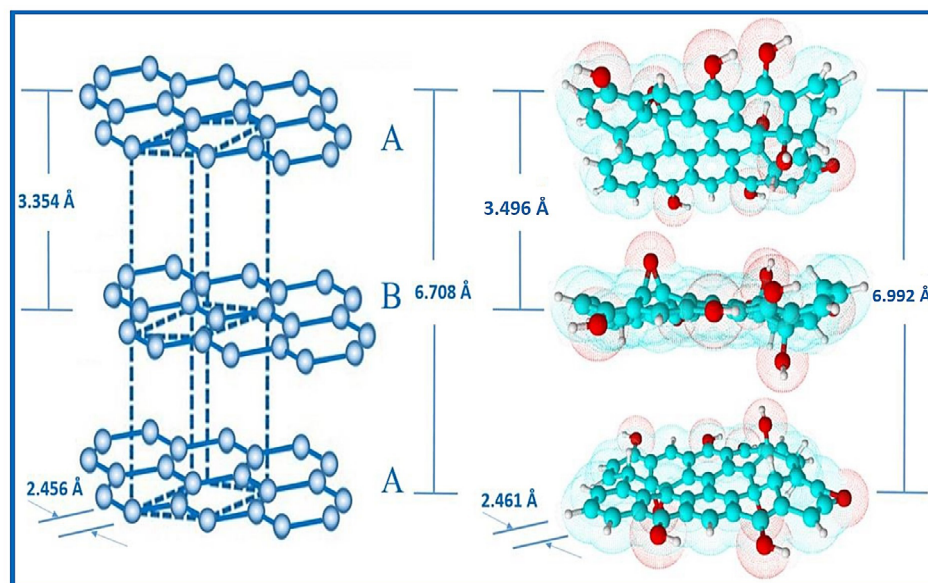


Figure 2. (a) Comparisons of geometric dimensions in graphite and rGO structures determined via XRD results analysis. (b) Typical Raman spectra in rGO sample

related to the elastic scattering due to structural defects such as grain boundaries, oxides, and sp^3 defects (C-O-C, C-OH, and C-H, respectively), and a D' band peak at 1593 cm^{-1} (from 1593 to 1620 cm^{-1}) due to the Raman inelastic scattering caused by the absorption or emission of phonons confined in defects, which can produce expansion and contraction of graphene oxide layers. The 2D, D+G, and 2D' band peaks at around 2697 , 2900 , and 3110 cm^{-1} , respectively, suggest that the stacking presence of many graphene layers with edges, defects, and sp^2 regions are prevalent features of rGO (Kajen *et al.*, 2013; Mineo *et al.*, 2013; Qiao *et al.*, 2005; Hyo *et al.*, 2014; Gregory *et al.*, 2014; Sánchez-Trujillo, 2023).

Figures 3a and b show the XPS spectra deconvolution analysis in an individual rGO nanoplatelet synthesized at 973 K carbonization temperature. It should be noted (Figure 3a) that the XPS spectra of high resolution in rGO nanoplatelets, exhibits oxidation presence and correspond to O1s, as expected, revealing the formation of hydroxyl groups, epoxy groups, and H_2O at 531.4 ± 0.2 , 532.3 ± 0.4 , and $535.9 \pm 0.5\text{ eV}$, respectively (Prías-Barragán *et al.*, 2022). Figure 3b corresponds to C1s and reveals the presence of C sp^2 , C sp^3 , hydroxyl groups, and C=O groups at 283.6 ± 0.1 , 284.9 ± 0.3 , 287.3 ± 0.4 , and $289.7 \pm 0.5\text{ eV}$, respectively, in the rGO sample. These values agree with previous works (Hoyos-Ariza *et al.*, 2023).

Figure 4a shows the SEM image of the individual rGO nanoplatelet electrically contacted by Ag nanowires deposited by the FEBID/FIBID technique and its geometric dimensions. These electrical connections allowed for measuring the temperature dependence with

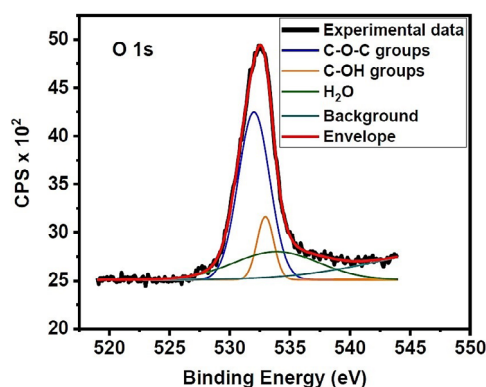


Figure 3. High resolution of XPS spectra in rGO nanoplatelet samples with 5.3% oxide coverage at (a) O1s high- and (b) low-binding C1s energies

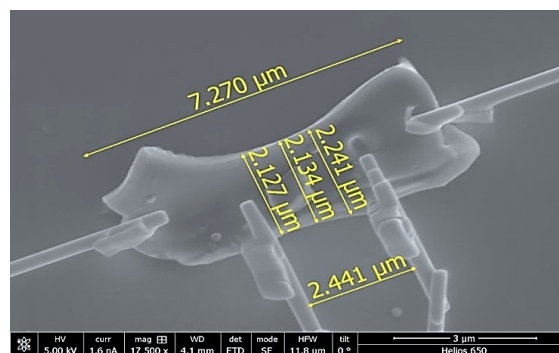


Figure 4. (a) SEM image of an individual rGO nanoplatelet electrically contacted by employing Ag nanowires with 300 nm thickness and the respective geometric dimensions. (b) Temperature dependence with the electrical resistivity in an individual rGO nanoplatelet, as shown in figure 4a. The inset in figure 4b shows the best fitting employing VRH-3D description.

the electrical resistivity in an individual rGO nanoplatelet (**Figure 4b**). The temperature decreased from 290 to 20 K, and the electrical resistivity increased from 0.001 to 0.0085 Ohm per meter, as in semiconductor materials. The inset in **figure 4b** shows the respective fitting description of the experimental data using the VRH-3D model (**Gross et al.**, 2016).

The inset in **figure 4b** plots $\ln(\sigma T^{1/2})$ as a function of $T^{-1/4}$ within 25 - 300 K, along with a best-fit line from the VRH-3D model. These results suggest that the charge transport in rGO is dominated by the Mott three-dimensional VRH transport behavior (**Gross et al.**, 2016; **Sánchez-Trujillo et al.**, 2023). In this case, the temperature dependence on conductivity can be expressed as in (6) (**Gross et al.**, 2016):

$$\sigma(T) = \frac{\sigma_o}{T^{1/2}} \exp \left[- \left(\frac{T_o}{T} \right)^{1/4} \right] \quad (6),$$

where σ_o and T_o are given by:

$$\sigma_o = \frac{3e^2 v_{ph}}{(8\pi)^{1/2}} \left[- \frac{N(E_F)}{\alpha K} \right]^{1/2} \quad (7)$$

and

$$T_o = \frac{16\alpha^3}{kN(E_F)} \quad (8),$$

where v_{ph} is the phonon frequency ($\approx 10^{13}$ Hz) at Debye temperature; $N(E_F)$ is the density of the localized electron states at Fermi level, and α is the inverse localization length of the wave function associated with the localized state. As shown in the graph, $\ln(\sigma T^{1/2})$ versus $T^{-1/4}$ in **figure 4** inset exhibits a linear behavior along the entire T range with a linearity factor of 0.997. From the slope and intercept values, parameters $T_o = 7.1 \times 10^4$ K and $\sigma_o = 8.8 \times 10^3$ Sm⁻¹ were obtained considering expressions (7) and (8), respectively. Using the values extracted for T_o and σ_o , the density of the localized states at Fermi Level $N(E_F) = 1.2 \times 10^{21}$ eV⁻¹cm⁻³ and an α value of 7.78×10^6 cm⁻¹ were calculated according to expressions (7) and (8) that revealed a magnitude order of importance in advanced electronics (**Gross et al.**, 2016).

Likewise, the localization length $\xi = 1/\alpha$ was determined at 1.3 nm in agreement with the average value of 1.6 nm determined by Raman in-plane crystal size (**Figure 1a-c**). Assuming a wave function confined in the graphitic domains of $D \sim \xi$ sizes and considering the linear dispersion relation for graphene as $E(k) = \hbar v_F k$, with v_F being the graphene Fermi velocity, and $k \sim 1/2\xi$, the bandgap energy value was estimated at 0.22 ± 0.02 eV, in good agreement with the value of 0.25 eV of oxidized graphene reported elsewhere (**Kajen et al.**, 2013). Temperature dependence on the band-gap energy of a single rGO nanoplatelet with 5.3% oxide concentration is presented in **Figure 5a-b**.

Given the low 5.3% average oxygen concentration value exhibited by an individual rGO nanoplatelet, here it is proposed that the $E_g(T)$ behavior in this sample can be estimated by considering $\sigma(T)$ as the inverse of the experimental data presented in **figure 4** inset and the following expression (**Prías-Barragán et al.**, 2018):

$$\sigma(T) = \sigma_G k T \exp \left[- \frac{E_g}{2kT} \right] \quad (9),$$

where σ_G is equal to 0.8×10^6 S/meV, which represents the shift ratio of the electrical conductivity in graphite by thermal energy unit in meV associated with the conductivity of graphite and independent of temperature; E_g is the band-gap energy and k is the Boltzmann constant. The exponential term is related to the temperature effect on the electrical response of the intrinsic semiconductor material, and the additional terms represent the temperature dependence on the electrical conductivity of graphite, as proposed by the Wallace model (**Wallace**, 1947). Thus, obtaining $E_g(T)$ from expression (9) can be written as (**Prías-Barragán et al.**, 2018):

$$E_g(T) = -2kT \ln \left[\frac{\sigma(T)}{\sigma_G kT} \right] + 2E_{g(300K)} \quad (10),$$

where two terms appear in the expression: the first one associated with the temperature effect on the band-gap energy of the rGO, as a semiconductor in the low-oxygen concentration regime (5.3% in an individual rGO nanoplatelet as already mentioned), and the second one corresponding to twice the band-gap energy value at room temperature (previously determined) required in expression (9), obtained from experimental data as a reference value to calibrate the curve (Gross *et al.*, 2016; Hoyos-Ariza *et al.*, 2023). Therefore, by replacing the values of $\sigma(T)$ calculated inversely from the experimental data presented in figure 4 and replacing $\sigma(T)$ in expression (10), it was possible to estimate the temperature influence on the band-gap energy of an individual rGO nanoplatelet (Figure 5a).

Figure 5a evidences that decreasing temperature from 290 to 25 K increased the band-gap energy from 0.117 to 0.285 eV, as expected in narrow band-gap semiconductor materials. The red solid line shows the data fit calculated using the Varshni model described in expression (1), with a square regression value at 0.99998 and $E_g(0 K) = 0.292$ eV as the best fit. The inset shows the same fit using the phenomenological models presented in the theory section. All the fit parameters obtained with expressions (1-5) are listed in table 1.

Figure 5b shows that the Viña model does not describe the experimental data as expected and has a square regression value of 0.83743. The other models can be related by means of these fit parameters: $\beta \cong \theta_B/2 \cong \theta_p$ and $\alpha \cong \alpha_p/2$ (Table 1). It was found that $E_g(T)$ can be described by the Varshni phenomenological expression (1), as expected for a

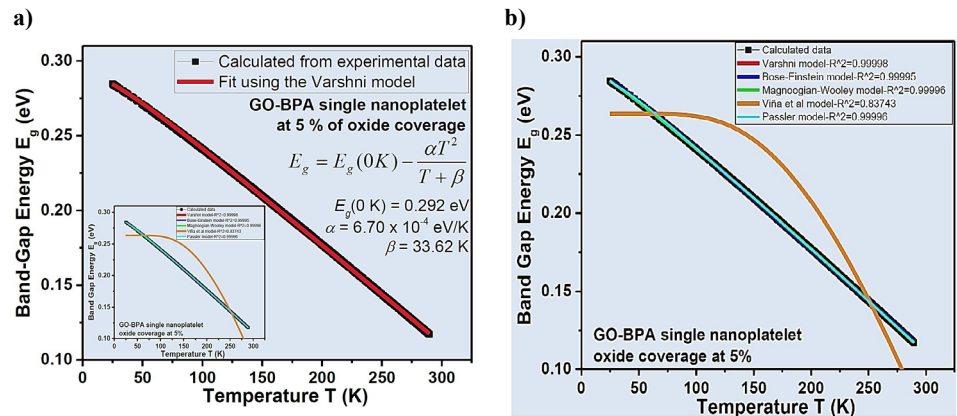


Figure 5. Temperature dependence with the band-gap energy values on an rGO nanoplatelet sample by employing (a) the Varshni model; the inset shows the fitting via other models; and (b) the Varshni, Bose-Einstein, Magnoogian-Wooley, Viña *et al.*, and Päsler models as given by expressions (1-5).

Table 1. List of fit parameters of the different models used

Models to describe $E_g(T)$				
Varshni	Bose-Einstein	Magnoogian-Wooley	Viña <i>et al.</i>	Päsler
$E_g(0 K) = 0.292$ eV	$E_g(0 K) = 0.288$ eV	$E_g(0 K) = 0.296$ eV	$E_g(0 K) = 0.263$ eV	$E_g(0 K) = 0.290$ eV
$\alpha = 6.70 \times 10^{-4}$ eV/K	$= 0.022$ eV	$V = 0.999$ eV/K	$b = 1.2$ eV	$\alpha_p = 3.34 \times 10^{-4}$ eV/K
$\beta = 33.62$ K	$\Theta_B = 67.49$ K	$\Theta = 1.1 \times 10^{-5}$ K	$\Theta = 721$ K	$\Theta_p = 67$ K
----	----	$U = 1$	----	$P = 1.95$
----	----	$S = 1$	----	----
$R^2 = 0.99998$	$R^2 = 0.99995$	$R^2 = 0.99996$	$R^2 = 0.83743$	$R^2 = 0.99996$

narrow band-gap semiconductor material, obtaining the Varshni coefficients at $E_g(0 K) = 0.292$ eV, $\alpha = 6.70 \times 10^{-4}$ eV/K, and $\beta \cong 34$ K; these values agree with the known order of magnitude of the Varshni coefficients reported for other narrow band-gap semiconductor materials like InAs ($E_g(0 K) = 0.417$ eV, $\alpha = 2.76 \times 10^{-4}$ eV/K, and $\beta = 93$ K) and InSb ($E_g(0 K) = 0.235$ eV, $\alpha = 3.90 \times 10^{-4}$ eV/K, and $\beta = 140$ K) (Prías-Barragán *et al.*, 2018).

Table 1 lists the fit parameters of the models used to describe the theoretical behavior of temperature dependence on the band-gap energy in an individual rGO nanoplatelet at 5.3% oxide concentration, as shown in **figure 1**.

The Varshni model describing electrical properties of rGO nanoplatelets suggests the temperature effect on the band-gap energy; however, the Varshni coefficients offer a few physics descriptions of the carriers or exciton interactions involved in some semiconductors, which explains why the Bose-Einstein model considers these effects in $E_g(T)$. Given that the R^2 values are similar in all the models used (**Table 1**), here, the Varshni phenomenological model was chosen to describe $E_g(T)$ since it contains fewer fitting parameters than the other phenomenological models and rGO is a polycrystalline material where disorder plays an important role; the Varshni model is simple for results interpretation without speculating on the physics involved in the description of $E_g(T)$.

From the result analyses in **figures 1** and **5**, it was established that the electrical behavior is dominated mainly by the presence of hydroxyl and epoxy bridges in rGO nanoplatelets, as reported by Hoyos-Ariza *et al.* (2023) employing first principle calculations via density functional theory (**Figure 3**). The hydroxyl and epoxy bridges can pull carbon atoms out-plane of the graphene locally (carbon out-plane defect), which results in uncompensated spin-charge density in GO systems (Prías-Barragán *et al.*, 2022); also, due to this defect, the carbon-carbon atoms average distance changes compared with the same distance in graphene or graphite (**Figure 2a**), with the opening of the band-gap energy appearing and rGO nanoplatelets exhibiting electrical behavior of narrow band-gap semiconductor (**Figures 2, 5**).

This effect of hydroxyl and epoxy bridges in rGO nanoplatelets is possibly responsible for the semiconductor behavior observed experimentally in rGO nanoplatelets. Theoretical and experimental results of the stable narrow band-gap semiconductor behavior induced by the adsorption of -OH and -O- atoms on graphene systems also suggest that rGO nanoplatelets can play a role in developing low-cost graphene and oxidized graphene-based technologies of advanced electronics of sensors and devices.

Conclusions

The theoretical and experimental evidence of temperature influence of the band-gap energy on rGO nanoplatelets, as in a narrow band-gap semiconductor system, is presented here. On the one hand, electrical measurement on individual rGO nanoplatelets revealed that electrical resistivity correlates with temperature as a semiconductor material, as expected. On the other hand, the temperature dependence with the band-gap energy on individual rGO nanoplatelets can be theoretically described by employing the Varshni model. Hence, these results, combined with the presence of hydroxyl and epoxy bridges in rGO nanoplatelets, may be explained as a semiconductor material given that the hydroxyl and epoxy bridges can pull carbon atoms out of the plane of the graphene locally (carbon out-plane defect) and, thus, produce the opening of the band-gap energy in the samples in the manner of a narrow band-gap system, as corroborated here experimentally. This effect is possibly responsible for the electrical properties observed in rGO nanoplatelets. Theoretical and experimental results of the stable narrow band-gap semiconductor behavior induced by the adsorption of -OH and -O- atoms on graphene systems also suggest that rGO nanoplatelets can play a role in developing low-cost graphene and oxidized graphene-based technologies of advanced electronics of sensors and devices.

Competing and financial interests

The author declares no competing financial interests.

Data availability statement

The datasets used and/or analyzed during the current study are available from the corresponding author upon reasonable request.

Acknowledgements

This work was funded partially by the Interdisciplinary Institute of Sciences at Universidad del Quindío, the Center of Excellence on Novel Materials at Universidad del Valle, and the Universidad del Quindío and MinCiencias project SGR BPIN: 2020000100600, internal code 1112.

References

- Abbas Z, Soomro, R. A., Kalmar, N. H., Mawada, T., Willander, M., Karakus, S. K., Ayben K. (2020). In Situ Growth of CuWO₄ Nanospheres over Graphene Oxide for Photoelectrochemical (PEC) Immunosensing of Clinical Biomarker. *Sensors*, 20, 148 1-10.
- Amir Faiz, M.S., Che Azurahaman, C.A., Yazid, Y., Suriani, A.B., Siti Nurul, A. M. (2020). Preparation and characterization of graphene oxide from tea waste and its photocatalytic application of TiO₂/graphene nanocomposite. *Journal Material Research Express*, 7, 015613 1-9.
- Arango Hoyos, B. E., Franco Osorio, H., Valencia Gómez, E. K., Guerrero Sánchez, J., Del Canto Palominos, A. P., Larrain, F. A., Prías-Barragán, J. J. (2023). Exploring the capture and desorption of CO₂ on graphene oxide foams supported by computational calculations. *Nature: Science Reports*, 13, 14476 1-15.
- Arias-Niquepa, R. A., Prías-Barragán, J. J., Ariza-Calderón, H., Rodríguez-García, M. E. (2019). Activated carbon obtained from bamboo: Synthesis, morphological, vibrational, and electrical properties and possible temperature sensor. *Physical Status Solidi A*, 2019, 1800422 1-11.
- Benevidesa, A.P., Campos, A.R., Vieira, L.C., Perez, C. dos Reis., Vargas, C.D. (2020). Reduced Graphene Oxide-Zinc Oxide Flower-Like Composite for Glass-Ionomer Materials Reinforcement. *Materials Research*, 23, e20190580 1-9.
- Geim, A.K., Novoselov, K.S. (2007). The rise of graphene. *Nat. Mater*, 6, 183-191.
- Geng, L., Wu, S., Zou, Y., Jia, M., Zhang, W., Yan, W., Liu, G. (2014). Correlation between the microstructures of graphite oxides and their catalytic behaviors in air oxidation of benzyl alcohol. *J. Colloid Interface Sci*, 421, 71-77.
- Geng, Y., Wang, S. J., Kim, J. K. (2009). Preparation of graphite nanoplatelets and graphene sheets. *Journal Colloid Interface Science*, 336, 592-598.
- Ghosh, R., Singh, A., Santra, S., Ray, S. K., Chandra, A., Guha, P. K. (2014). Highly sensitive large-area multi-layered graphene-based flexible ammonia sensor. *Sens. Actuators B*, 205, 67-73.
- Grande, L., Chundi, V.T., Wei, D., Bower, C., Andrew, P., Ryhänen, T. (2012). Graphene for energy harvesting/storage devices and printed electronics. *Particuology*, 10, 1-8.
- Gregory Thien S H, Pandikumar, A., Nay Ming, H., Hong Ngee, L. (2014). Highly exposed {001} facets of titanium dioxide modified with reduced graphene oxide for dopamine sensing. *Nature: Science Reports*, 4, 5044 1-8.
- Gross, K., Prías-Barragán, J. J., Sangiao, S., Lajaunie, L., Arenal, R., Ariza-Calderón, H., Prieto, P. (2016). Electrical conductivity of oxidized-graphenic nanoplatelets obtained from bamboo: effect of the oxygen content. *Nanotechnology*, 27, 365708 1-10.
- He, L. X., Tjong, S. C. (2013). Zener tunneling in conductive graphite/epoxy composites: Zener tunneling in conductive graphite/epoxy composites: Dielectric breakdown aspects. *Express Polymers Letters*, 7, 375-382.
- He, Z., Xia, H., Zhou, X., Yang, X., Song, Y., Wang, T. (2011). Raman study of correlation between defects and ferromagnetism in graphite. *J. Phys. D: Appl. Phys*, 44, 085001-9.
- Hoyos-Ariza, F. A., Prías-Barragán, J. J., Galván, D. H., Guerrero-Sánchez, J., Ariza-Calderón, H. (2023). Graphene nanostructures functionalization: Hydrogen bonds and oxide coverage effect. *Materials Today Communications*, 36, 106861 1-11.
- Hyo, J. K., Sung-Min, L., Yoon-Suk, O., Young-Hwan, Y., Young Soo, L., Dae, Ho Y., Changgu, L., Jong-Young, K., Rodney, S. (2014). Unoxidized Graphene/Alumina Nanocomposite: Fracture- and Wear-Resistance Effects of Graphene on Alumina Matrix. *Nature: Science Report*, 4, 5176 1-10.
- ISO Technical specification (2008). Nanotechnologies — Terminology and definitions for nano-objects — Nanoparticle, nanofibre and nanoplatelet. *ISO/TS 2008*, 27687:2008(E).

- Jia, G., Zhang, W., Jin, Z., An, W., Gao, Y., Zhang, X., Liu, J.** (2014). Electrocatalytically Active MOF/Graphite Oxide Hybrid for Electrosynthesis of Dimethyl Carbonate. *Electrochimica Acta*, 144, 1-6.
- Jiang, H., Chen, P., Zhang, W., Luo, S., Luo, X., Peter, C. Au., Li, M.** (2014). Deposition of nano Fe₃O₄@mZrO₂ onto exfoliated graphite oxide sheets and its application for removal of amaranth. *Appl. Surf. Sci.*, 317, 1080-1089.
- Kajen, R. S., Chandrasekhar, N., Pey, K. L., Vijila., C, Jaiswal M., Saravanan, S., Andrew M H Ng., Wong, C. P., Loh, K.P.** (2013). Trap Levels in Graphene Oxide: A Thermally Stimulated current study. *ECS Solid State Letters*, 2, M17-M19.
- Kigozi, M., Koech, R. K., Kingsley, O., Ojeaga, I., Tebandeke, E., Kasozi, G. N., Onwualu, A. P.** (2020). Synthesis and characterization of graphene oxide from locally mined graphite flakes and its supercapacitor applications. *Results in Materials*, 7, 100113 1-12.
- Kim, M., Kang, G. H., Park, H. W., Park, Y. B., Park, Y. H., Yoon, K. H.** (2012). Design, Manufacturing, and Characterization of High-Performance Lightweight Bipolar Plates Based on Carbon Nanotube-Exfoliated Graphite Nanoplatelet Hybrid Nanocomposites. *Journal of Nanomaterials*, 159737, 1-8.
- Krystek, W., Malikova, L., Pollak, F. H.** (1995). Contactless electroreflectance study of temperature dependence of fundamental band gap of ZnSe. *Acta Physica Polonica A*, 88 (5), 1013-1017.
- Kuzemsky, A. L.** (2013). Unconventional and exotic magnetism in carbon-based structures and related materials. *Journal of Modern Physics B*, 27, 1330007 1-40.
- Kyzas G. Z., Bikiaris D. N., Deliyanni E. A.** (2014). Advanced low-swelling chitosan/graphite oxide-based biosorbents. *Mater. Lett.* 128, 46-49.
- Li, Fenfen., Linyu, L., Yunxuan, W.** (2020). A Review on the Contemporary Development of Composite Materials Comprising Graphene/Graphene Derivatives. *Advances in Materials Science and Engineering*, 2020, 1-16.
- Liu, Z., Duan, X., Cheng, H., Zhou, J., Zhou, X., Yuan, W.** (2015). Synthesis of platinum/graphene composites by a polyol method: The role of graphite oxide precursor surface chemistry. *Carbon*, 89, 93-101.
- Llatser, I., Kremers, C., Cabellos-Aparicio, A., Jornet, J.M., Alarcon, E., Chigrin, D. N.** (2012). *Photonics and Nanostructures – Fundamentals and Applications*, 10, 353-358.
- Lobato, B., Wendelbo, R., Barranco, V., Centeno, T. A.** (2014). Graphite Oxide: An Interesting Candidate for Aqueous Supercapacitors. *Electrochimica Acta*, 149, 245-251.
- Makarova, T. L., Shelankov, A. L., Serenkov, I. T., Sakharov, V. I., Boukhalov, D. W.** (2011). Anisotropic magnetism of graphite irradiated with medium-energy hydrogen and helium ions. *Physical Reviews B*, 83, 085417 1-8.
- Matsuo, Y., Ueda, K.** (2014). Pyrolytic carbon from graphite oxide as a negative electrode of sodium-ion battery. *Journal of Power Source*, 263, 158-162.
- Mineo, H., Kondo, H., Hori, M.** (2013). Graphene Nanowalls. *In Tech Chapter 9*. 235-260.
- Mishra, A. K., Ramaprabhu, S.** (2012). Graphene-based nano-patch antenna for terahertz radiation. *Chem. Eng. J.*, 187, 10-15.
- Mizoguchi, T., Misaki, H., Shintaro, I., Michio, K.** (2020). Free Standing Graphene Oxide Membrane with Epoxy Groups for Water Purification. *Chemical Letters*, 49, 376-378.
- Mu, X., Wu, X., Zhang, T., Go, D. B., Luo, T.** (2014). Thermal Transport in Graphene Oxide –From Ballistic Extreme to Amorphous Limit. *Nature: Science Reports*, 4, 3909 1-9.
- Naser, A. A., Al-Sawaad, H. Z., Al-Mubarak, A. S.** (2020). Novel graphene oxide functionalization by urea and thiourea, and their applications as anticorrosive agents for carbon steel alloy in acidic medium. *J. Mater. Environ. Sci*, 11, 3 404-420.
- Newman, L., Rodrigues, A. F., Jasim Dhifaf, A., Vacchi, I. A., Menard-Moyon, C., Bianco, A., Busy, C., Kostarelos, K.** (2020). Nose-to-Brain translocation and cerebral biodegradation of thin graphene oxide nanosheets. *Cell Reports Physical Science*, 1, 100176 1-23.
- Novoselov, K. S., Geim, A. K., Morozov, S. V., Jiang, D., Katsnelson, M.I., Grigorieva, I. V., Dubonos, S.V., Firsov, A. A.** (2005). Two-dimensional gas of massless Dirac fermions in graphene. *Nature*, 438, 197-200.
- Novoselov, K. S., Geim, A. K., Morozov, S. V., Jiang, D., Zhang, Y., Dubonos, S. V., Grigorieva, I. V., Firsov, A. A.** (2004). Electric Field Effect in Atomically Thin Carbon Films. *Science*, 306, 666-669.
- O'Donnell, K. P., Chen, X.** (1991). Temperature dependence of semiconductor band gaps. *Appl. Phys. Letters*, 58, 2924-2926.

- Pässler, R.** (1997). Basic model relations for temperature dependencies of fundamental energy gaps in semiconductors. *Phys. Stat. Sol. B*, 200, 155-172.
- Petit, C., Bandosz, T. J.** (2015). Engineering the surface of a new class of adsorbents: Metal–organic framework/graphite oxide composites. *J. Colloid Interface Sciences*, 447, 139-151.
- Prías-Barragán, J. J.** (2018). Transport mechanisms study in graphite oxide platelets obtained from bamboo for possible applications in electronic. Doctoral Thesis, University of Valle, Colombia, 1, 1-209.
- Prías-Barragán, J. J., Echeverry-Montoya, N. A., Ariza-Calderón, H.** (2015). Fabricación y caracterización de carbón activado y de nanoplaquetas de carbón a partir de Guadua angustifolia Kunth para aplicaciones en electrónica. *Revista de la Academia Colombiana de Ciencias Exactas, Físicas y Naturales*, 39, 444-449.
- Prías-Barragán, J.J., Gross, K., Ariza-Calderón, H., Prieto, P.** (2016). Synthesis and vibrational response of graphite oxide platelets from bamboo for electronic applications. *Phys. Status Solidi A*, 213, 85-90.
- Prías-Barragán, J. J., Gross, K., Ariza-Calderón, H., Prieto, P.** (2018). Transport mechanisms study in graphene oxide multilayers obtained from bamboo as source material and possible applications in electronic. *Revista de Divulgación Científica y Tecnológica, del Instituto Interdisciplinario de las Ciencias de la Universidad del Quindío*, 1, 9-47.
- Prías-Barragán, J. J., Gross, K., Ariza-Calderón, H., Prieto, P.** (2019). Graphene Oxide Multilayers Obtained from Bamboo: New Synthesis Method, Basic Properties, and Future Electronic Applications. *Wiley Scrivener Publishing LLC, London UK*. 8, 191-236.
- Prías-Barragán, J. J., Gross, K., Ariza-Calderón, H., Prieto, P.** (2019). Graphene oxide multilayers: Synthesis, properties and possible applications in electronics. *Latin American Electron Devices Conference IEEE 1*, 61-64.
- Prías-Barragán, J.J., Gross, K., Ariza-Calderón, H., Prieto, P., Di Giorgio, C., Bobba, E., Cucolo, A.M.** (2021). Room-temperature ferromagnetism in oxidized-graphenic nanoplatelets induced by topographic defects. *Journal of Magnetism and Magnetic Materials*, 524, 167664 1-11.
- Prías-Barragán, J. J., González-Hernández, R., Hoyos-Ariza, F., Ramírez, J. G., Ibarra, M. R., Prieto, P.** (2022). Magnetism in graphene oxide nanoplatelets: The role of hydroxyl and epoxy bridges. *Journal of Magnetism and Magnetic Materials*, 541, 168506 1-8.
- Prías-Barragán, J. J., Gross, K., Perea, J.D., Killilea, N., Heiss, W., Brabec, C. J., Ariza-Calderón, H., Prieto, P.** (2020). Graphene Oxide Thin Films: Synthesis and Optical Characterization. *Chemistry Select*, 5, 11737-11744.
- Prusty, G., Swain, S. K.** (2012). Dispersion of expanded graphite as nanoplatelets in a copolymer matrix and its effect on thermal stability, electrical conductivity and permeability. *New Carbon Materials*, 27, 271-277.
- Qiao, W. M., Song, Y., Huda, M., Zhang, X., Yoon, S. H., Mochida, I., Katou, O., Hayashi, H., Kawamoto, K.** (2005). Development of carbon precursor from bamboo tar. *Carbon*, 43, 3021-3025.
- Rao, C. N. R., Ramakrishna, Matte H. S., Subrahmanyam, K. S., Urmimala, M.** (2012). Unusual magnetic properties of graphene and related materials. *Chem. Sci.* 3, 45-52.
- Rozploch, F., Patyk, J., Stankowski, J.** (2007). Graphenes Bonding Forces in Graphite *Acta Phys. Polonica. A*, 112, 557-563.
- Rui Chen, Quan-Lin, Ye., He, T. C., Wu, T., Sun, H. D.** (2011). Uniaxial tensile strain and exciton–phonon coupling in bent ZnO nanowires. *Applied Physics Letters*, 98, 241916-1-3.
- Sachdeva, H.** (2020). Recent advances in the catalytic applications of GO/rGO for green organic synthesis. *Green Processing and Synthesis*, 9, 515-537.
- Sanchez-Trujillo, D. J., Osorio-Maldonado, L. V., Prías-Barragán, J. J.** (2023). Temperature dependence of electrical conductivity and variable hopping range mechanism on graphene oxide films. *Nature: Science Report*, 13(4810), 1-12.
- Sangwan, V. K., Southard, A., Moore, T. L., Ballarotto, V. W., Hines, D. R., Fuhrer, M. S., Williams, E. D.** (2011). Transfer printing approach to all-carbon nanoelectronics. *Nanoelectronics Microelectron. Eng.* 88, 3150-3154.
- Singh, A., Chandra, A.** (2013). Graphite oxide/polypyrrole composite electrodes for achieving high energy density supercapacitors. *J. Appl. Electrochem.* 43, 773-782.
- Tang, L., Li, X., Ji, R., Teng, K. S., Tai, G., Ye, J., Wei, C., Lau, S. P.** (2012). Bottom-up synthesis of large-scale graphene oxide nanosheets. *J. Mater. Chem.* 22, 5676-5683.

- Tang, Q., Wu, J., Li, Q., Lin, J.** (2008). High conducting multilayer films from poly (sodium styrene sulfonate) and graphite nanoplatelets by layer-by-layer self-assembly. *Polymer*, *49*, 5329-5335.
- Varshni, Y. P.** (1967). Temperature dependence of the energy gap in semiconductors. *Physica*, *34*, 149-154.
- Vina, L., Igothetidis, S., Cardona, M.** (1984). Temperature dependence of the dielectric function of germanium. *Physical Review B*, *30* (4), 1979-1991.
- Virendra, S., Joung, D., Zhai, L., Das, S., Khondaker, S. I., Seal, S.** (2011). Graphene based materials: Past, present and future. *Progress in Materials Science* *56*, 1178-1271.
- Wallace, P.R.** (1947). The band theory of graphite. *Physical Review*, *71*(9), 622-634.
- Wang, Y., Yingbo, Q., Yu, S., Meng, Z., Shaobo, D.** (2020). A study on preparation of modified Graphene Oxide and flame retardancy of polystyrene composite microspheres *Designed Monomers and Polymers*, *23*, 1-15.
- Wei, T., Fan, Z., Zheng, C., Yao, C., Li, W.** (2009). Movement-induced voltage properties of stable graphite nanoplatelet suspensions. *Material Letters*, *63*, 1608-1610.
- Xue, C., Zou, J., Sun, Z., Wang, F., Han, K., Zhu, H.** (2014). Graphite oxide/functionalized graphene oxide and polybenzimidazole composite membranes for high temperature proton exchange membrane fuel cells. *International Journal Hydrogen Energy*, *39*, 7931-7939.
- Zhang, Bo., Li, Q., Cui, T.** (2012). Título del Artículo. *Biosensors Bioelectron*, *31*, 105-109.
- Zou, B. K., Zhang, Y. Y., Wang, J. Y., Liang, X., Ma, X. H., Chen, C. H.** (2015). Hydrothermally enhanced MnO/reduced graphite oxide composite anode materials for high performance lithium-ion batteries. *Electrochimica Acta*, *167*, 25-31.